



Wellbore stability analysis using integrated geomechanical modeling: a case study from the Sarvak reservoir in one of the SW Iranian oil fields

Mohsen Ezati¹ · Mehran Azizzadeh^{1,2} · Mohammad Ali Riahi³ · Vahidoddin Fattahpour⁴ · Javad Honarmand¹

Received: 5 September 2019 / Accepted: 22 January 2020 / Published online: 4 February 2020
© Saudi Society for Geosciences 2020

Abstract

In this study, an integrated geomechanical analysis was carried out for the Sarvak carbonate reservoir in three wells of one of the oil fields in Abadan Plain, SW Iran. The static Young's modulus (E_S), unconfined compressive strength (UCS), cohesion (C), and angle of internal friction (Φ) were determined directly, using rock mechanics tests. Subsequently, some correlations were introduced based on tests-to-logs relationships. The 1D geomechanical models were constructed for three wells in the north, center, and south of the studied field. The results show that the stress state is not uniform for the studied wells, as it is strike-slip normal in northern well, strike-slip in central well, and strike-slip reverse in southern well. Likewise, the stability of the wells was evaluated using Mohr-Coulomb and Mogi-Coulomb criteria, and it was observed that the Mogi-Coulomb criterion could more accurately estimate the breakout pressure. According to the recognized borehole breakouts in image logs, the S_{Hmax} direction is to NE-SW in all three wells. Based on the wellbore stability analysis, it was concluded that the more stable directions for drilling are NW-SE in the northern part, E-W and N-S in the central part, and NE-SW in the southern part of the studied oil field.

Keywords Geomechanical modeling · Stress state · Wellbore stability · Sarvak Formation · Abadan Plain · SW Iran

Nomenclature

BS	Bit size
C	Cohesion
CAL	Caliper
DSI	Dipole shear sonic imager
DST	Drill stem test
DT	Slowness of compressional wave
DT _m	P wave slowness in shale with zero porosity
DT _{ml}	P wave slowness in drilling mud

E	Young's modulus
FMI	Fullbore formation microimager
Fullset logs	Caliper, bit size, gamma ray, bulk density, neutron porosity, slowness of compressional wave, photoelectric factor, and resistivity logs
g	Earth's gravitational acceleration
GR	Gamma ray
MDT	Modular dynamics tester
NCT	Normal compaction trend
NPHI	Neutron porosity
OBMI	Oil-base microimager
pcf	Pound per cubic foot
PEF	Photoelectric factor
PHIE	Effective porosity
PP	Pore pressure
P _{pg}	Pore pressure gradient
P _{PHyd}	Hydrostatic pore pressure gradient
P _w	Drilling mud pressure
P _{wb}	Drilling mud pressure which causes borehole breakouts
P _{wf}	Drilling mud pressure which causes induced fractures

Responsible editor: Zeynal Abiddin Erguler

✉ Mohsen Ezati
ezatim@ripi.ir; mohsenezati7@yahoo.com

✉ Mehran Azizzadeh
azizzadehm@ripi.ir

- ¹ Research Institute of Petroleum Industry (RIPI), Tehran, Iran
- ² Petroleum Geology Dept., Center for Exploration & Production, Research Institute of Petroleum Industry (RIPI), West Blvd., Azadi Sport Complex, P.O.Box: 14665-1998, Tehran, Iran
- ³ Institute of Geophysics, University of Tehran, Tehran, Iran
- ⁴ School of Mining Engineering, University of Tehran, Tehran, Iran

RFT	Repeat formation tester
RHOB	Bulk density
S_1	Maximum principal stress
S_2	Intermediate principal stress
S_3	Minimum principal stress
S_{Hmax}	Maximum horizontal stress
S_{Hmin}	Minimum horizontal stress
$S_{m,2}$	Effective mean stress
S_n	Normal stress
S_V	Vertical stress (overburden stress)
TS	Tensile strength
UBI	Ultrasonic borehole imager
UCS	Unconfined compressive strength
V_P	Compressional wave velocity
V_S	Shear wave velocity
τ_{oct}	Octahedral shear stress
μ	Coefficient of internal friction
ϵ_x	tectonic strain on x plane
ϵ_y	tectonic strain on y plane
α	Biot's coefficient
ν	Poisson's ratio
ν_d	Dynamic Poisson's ratio
ρ	Density of rock
ρ	Overburden average density
σ_1	Maximum principal effective stress
σ_3	Minimum principal effective stress
σ_r	Radial stress
σ_z	Axial stress
$\sigma^{\Delta T}$	Thermal stress
σ	Tangential stress
τ	Shear stress
Φ	Angle of internal friction

Introduction

Geomechanical analysis plays an important role in the various stages of exploration and exploitation of hydrocarbon reservoirs (Hui and Deli 2005). In the exploratory stage, geomechanical models are very important in predicting pore pressure and estimating in situ stresses (Hui and Deli 2005). Likewise, in drilling stage, geomechanical properties have critical impact on bit selection, optimization of the drilling path, casing design, and determining the safe mud weight window (Zhang et al. 2010; Karakus and Perez 2014).

The main elements of a geomechanical model are rock mechanical properties, pore pressure, and in situ stress state (Plumb 1994). Rock mechanical tests are prerequisite for any geomechanical investigation (Plumb 1994). In recent years, a variety of rock mechanics' tests developed and used worldwide in petroleum industry. However, because of limited availability of core samples for each project, carefully selected lab tests are of great importance. Unconfined compressive strength (UCS) is

used to evaluate the wellbore stability, probability of sand production (Santarelli et al. 1989), and determination of the range of in situ stresses (Zoback et al. 2003). It is measured directly using uniaxial compressive test on core samples. Also, there are some empirical correlations to estimate this parameter (Chang et al. 2006). Determining the magnitudes and directions of stresses is the key component of a geomechanical model. Image logs are essential tools for determining in situ stresses direction (Ezati et al. 2014; Ezati et al. 2019b).

The vertical and azimuthal resolution of FMI image log is 0.5 mm which makes it able to detect very small and narrow events like tiny laminations, stylolites, solution seams, and fractures.

Cohesion (C) and angle of internal friction (Φ) are critical parameters to evaluate the wellbore stability and determine the optimal drilling mud weight (Zhang et al. 2010). These parameters are the intrinsic characteristics of rocks and could be estimated by several empirical relationships (e.g., Plumb 1994; Jaeger et al. 2009).

Pore pressure is required to evaluate in situ stresses and the safe window of drilling mud (Zoback 2010). The formation pore pressure can be measured directly (in separate points) using MDT (Modular Dynamics Tester), RFT (Repeat Formation Tester), and DST (Drill Stem Test) tools (Zoback 2010). In addition, the pore pressure is estimated using empirical relationships based on petrophysical logs in a continuous manner (Zhang 2011). Then, the estimated values can be calibrated using the directly measured values.

The stability of the wellbores has been studied in different literature, worldwide (Roegiers 2002; Awal et al. 2001; Chen et al. 2003; Al-Ajmi and Zimmerman 2006; Akhtarmanesh et al. 2013; Li et al. 2017., Zhou et al. 2018). However, challenges such as complete mud losses and large washouts still happen. Geomechanical studies in Iran were mainly performed for the Asmari Formation (Yaghoubi and Zeinali 2009; Fattahpour et al. 2012; Darvish et al. 2015; Ghafoori et al. 2018; Lashkaripour et al. 2018), which is the main Iranian oil reservoir (Motiei 1993). In addition, various geomechanical aspects of Dalan and Kangan formations have been studied. The stress state (Haghi et al. 2013; Aghajanpour et al. 2017), pore pressure (Azadpour et al. 2015), and rock mechanical properties (Mehrgini et al. 2016) were analyzed for these formations in one of the gas fields of Southern Iran.

Najibi et al. (2015) presented a number of relationships to estimate UCS and E_s for the Asmari and Sarvak Formations commonly in the Dezful Embayment. In their study, V_P (compressional wave velocity) and V_S (shear wave velocity) in ambient conditions were used for the elastic modules calculation. Najibi et al. (2017), using 1D geomechanical modeling, estimated the principal stresses in one of the Dezful Embayment wells for the Bangestan reservoir. Rajabi et al. (2010) determined the horizontal stress directions in two wells in the Abadan Plain.

The Sarvak Formation (Albian to Turonian) contains more than 20% of the oil reserves of Iran (Motiei 1993). It is one of the main reservoirs in the Abadan Plain, SW Iran (Abdollahie-Fard et al. 2006). However, Sarvak reservoir has not been accurately evaluated from a geomechanical point of view, and in situ stress state is almost unknown in this region. In this study, a comprehensive data set from three wells was used to evaluate the rock mechanical parameters, in situ stresses, and wellbore stability in the Sarvak Formation in one of the oil fields in Abadan Plain. The final results can be considered for the future development plans and field management.

Geological setting

The studied field is an N-S-trending anticline, which is located in the Abadan Plain, SW Iran. The positions of the three studied wells are shown in Fig. 1a.

The Abadan Plain shows three main structural trends: N-S, NE-SW, and NW-SE which are related to the deep-seated faults (Abdollahie-Fard et al. 2006). The associated structures to these trends are relevant to reactivation of basement-rooted normal faults which caused forced folding in overlaying sediments (Abdollahie-Fard et al. 2006).

The generation of the studied anticline associated with a complex horst system. Seismic data of this anticline show steep faulting in the core of the structure (Abdollahie-Fard et al. 2006). Arabian N-S-trending, basement-involved horst systems have been named differently, according to their geographical location, such as Kuwait High, Burgan High, Khurais-Burgan anticline, and Basrah High in Iraq (Abdollahie-Fard et al. 2006). Several oil fields are located along this regional trend in Saudi Arabia, Kuwait, and Iraq. In SW Iran, the N-S trend is identified in the Abadan Plain (Abdollahie-Fard et al. 2006).

The Sarvak Formation was deposited in upper Cretaceous during late Albian to early Turonian (Omidvar et al. 2014). In Abadan Plain, the Sarvak Formation is overlain by the Lafan shale with an unconformity, and its lower contact with Kazhdumi Formation is gradual. The Sarvak Formation comprises thick limestone and dolomitic limestone, with minor clayey and argillaceous intervals, reaching totally 600–700 m in thickness (Assadi et al. 2016, Fig. 1b).

In the Abadan Plain, natural fractures have little expansion in the Sarvak Formation (Ezati et al. 2018; Ezati et al. 2019a). Diagenetic studies of the Sarvak Formation in Abteymour field (one of the Southwestern Iranian fields) show that the

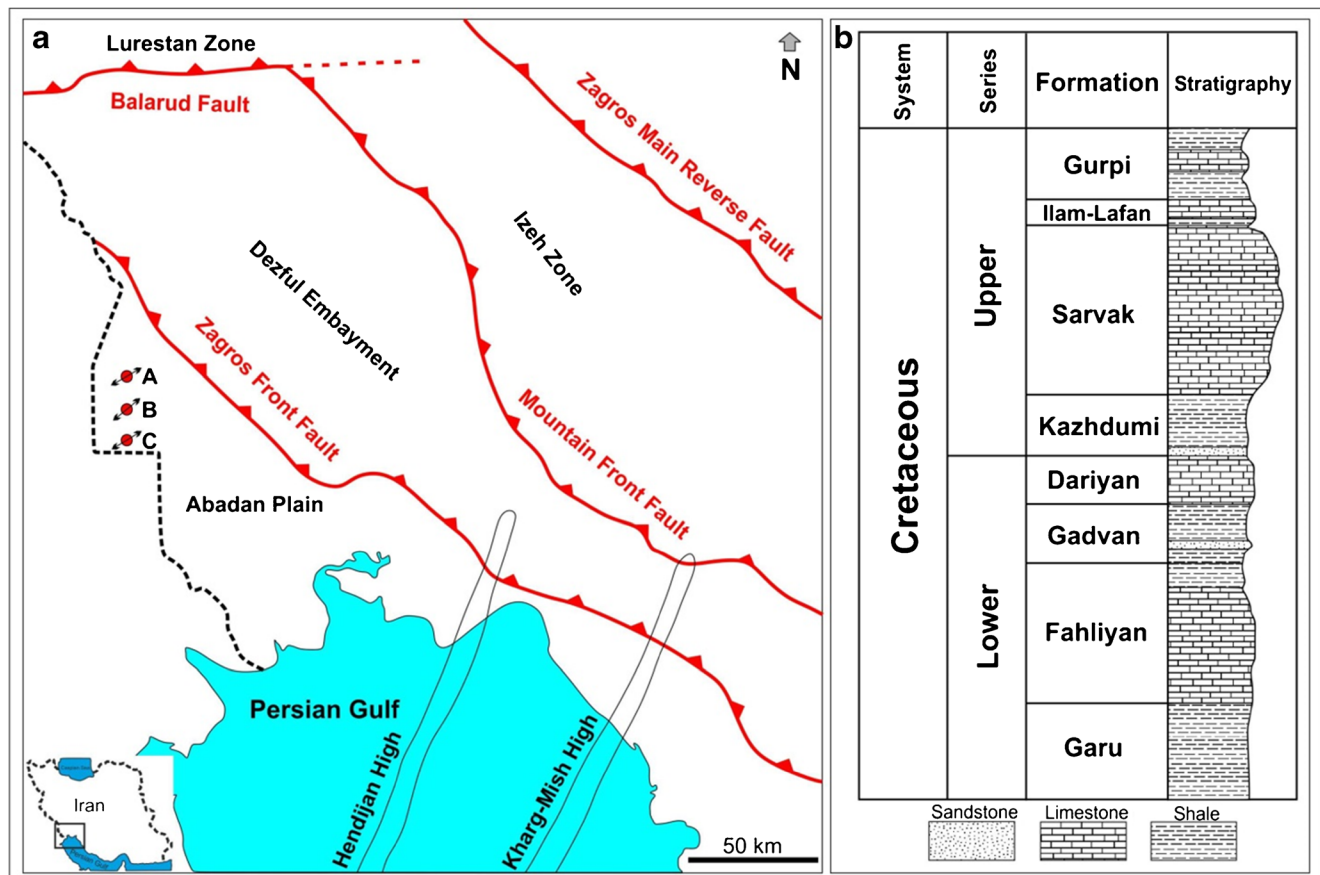


Fig. 1 a The three studied wells (shown as A, B, and C) in Abadan Plain, SW Iran. The S_{Hmax} directions in the studied wells are indicated by arrows. b The Cretaceous stratigraphic column of the Abadan Plain

reservoir quality of this reservoir is enhanced both by dissolution and dolomitization (Rahimpour-Bonab et al. 2012). Dissolution features in the Sarvak Formation are often caused by outcrops of this formation due to tectonic activities (Rahimpour-Bonab et al. 2013). Results of facies analysis in some SW Iranian fields indicate a homoclinal ramp-type carbonate platform for the Sarvak Formation (Mehrabi and Rahimpour-Bonab 2014). Also, Mehrabi et al. 2015 showed that the large-scale variations in facies and thicknesses of the Sarvak Formation are controlled by regional tectonic evolution and sea-level changes during the Upper Cretaceous.

Available data

The studied wells are situated in northern (well-A), central (well-B), and southern (well-C) parts of the studied field. The top and base depths of the Sarvak Formation in well-A, well-B, and well-C are 3708–4331, 3720–4371, and 3631–4269 m, respectively. A summary of the data resource of this study is presented in Table 1.

Fullset logs were used for petrophysical evaluation, pore pressure estimation, overburden stress measurement, and the elastic modulus calculation. FMI (Fullbore Formation Microimager), UBI (Ultrasonic Borehole Imager), and OBMI (Oil-Base Microimager) image logs were utilized to detect the wellbore wall failures. DSI data was used to extract V_S for the elastic modulus measurement. MDT pressure points were considered to calibrate the pore pressure curves. Also, 27 plug samples were taken from the Sarvak reservoir for the geomechanical tests.

Methods

1D geomechanical modeling

A Mechanical Earth Model (MEM) is a numerical depiction of the geomechanical properties of a formation (Ali et al. 2003). In addition to property distribution (e.g., lithology, density, porosity), the MEM model includes pore pressures, stress state, and rock mechanical characteristics.

Table 1 Summary of data used in this study

Data	Well-A	Well-B	Well-C
Fullset logs	✓	✓	✓
Dipole shear sonic imager (DSI)	✓	✓	✓
Image logs	✓	✓	✓
MDT	✓	✓	✓
Uniaxial and triaxial tests on core	✓		
Drilling report	✓	✓	✓

1D geomechanical model is constructed based on the well data. The well logging data such as shear and compression waves velocity, density, caliper, porosity, and gamma ray are used to present mechanical properties and stress state near wellbore (Ali et al. 2003). This model can be used to investigate the mechanical properties of rocks and in situ stresses near the wellbore (Ali et al. 2003).

Dynamic rock elastic properties

The dynamic Young's modulus (E_d) and dynamic Poisson's ratio (ν_d) were calculated using V_P , V_S , and density of rock (ρ) as follows (Fjaer et al. 2008):

$$E_d = \rho V_S^2 \frac{3V_P^2 - 4V_S^2}{V_P^2 - V_S^2} \quad (1)$$

$$\nu_d = \frac{V_P^2 - 2V_S^2}{2(V_P^2 - V_S^2)} \quad (2)$$

Typically, high elastic values are obtained in the dynamic condition, so dynamic values should be converted to static values by performing mechanical tests (Zoback 2010).

The rock mechanical tests

In this study, 27 vertical plug samples were taken from the Sarvak reservoir cores of well-A (from the 3710.25 to 3950.57-m depths) for the rock mechanical tests. The diameters of the plugs are 1.5 in., and their lengths are twice the diameter. Sixteen plugs were selected for uniaxial compression test, and 11 plugs were used for multistage triaxial compression test.

The ASTM D3148–93 standard was followed for the uniaxial test. For the uniaxial test, the plugs were placed in a loading frame. Axial load was increased on the specimen at a constant and continuous rate, while axial and lateral deformations were monitored as a function of load. Figure 2a shows the stress-strain diagram for one of the plugs which was failed with a shear fracture. The E_S and UCS were determined for all 16 plugs. The results of uniaxial test are shown in Table 2.

The ASTM 2664-95a standard was considered for the triaxial test. For the multistage triaxial test, the plugs were placed in a triaxial loading chamber (cell), subjected to confining pressure. At least, three triaxial compression tests (with different confining pressure) were accomplished on the plugs. In Fig. 2b, triaxial test is shown along with its Mohr circles. A shear fracture has been developed in the plug specimen (Fig. 2b).

The C and Φ were determined using the triaxial tests. The results of the triaxial test are shown in Table 3.

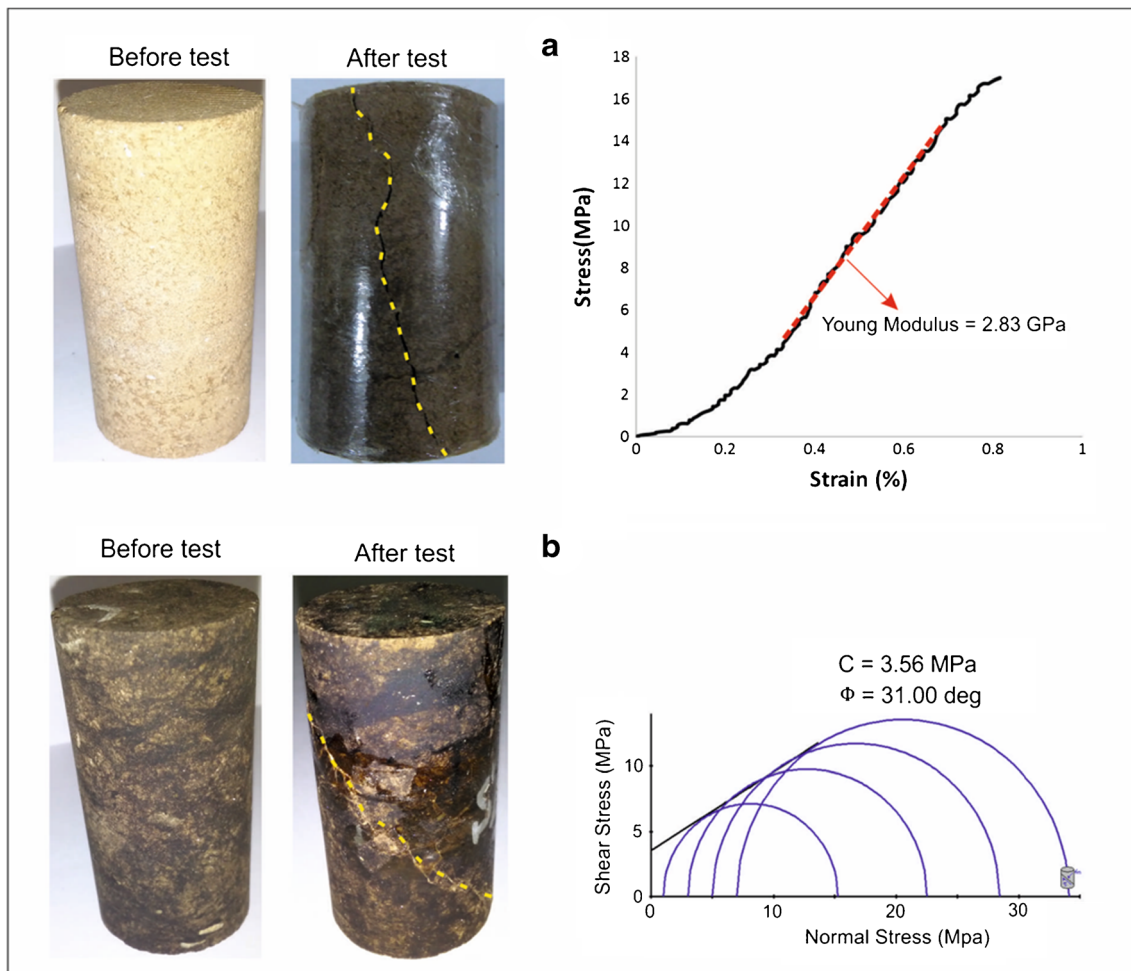


Fig. 2 a S28 plug sample before and after uniaxial testing and its stress-strain diagram. b S11 plug sample before and after multistage triaxial test. The shear fractures of these tests are highlighted by the yellow dashed lines

Log data calibration with the rock mechanical tests

Throughout the cored section of well-A, E_s and UCS were determined using uniaxial test on 16 plug samples from Sarvak reservoir. In the next step, the E_d was calculated using the V_B , V_S (from DSI data), and density logs. The relationship between the static and dynamic Young’s modulus is as follows (also, see Fig. 3a):

$$E_s = 0.0173E_d^2 - 0.9715E_d + 17.274 \tag{3}$$

In order to estimate UCS continuously, UCS values were compared with some of the rock properties (such as porosity, E_s , and E_d), and it was observed that UCS has the best correlation with the E_d (Fig. 3b):

$$UCS = 0.0635E_d^2 - 3.2185E_d + 55.949 \tag{4}$$

The C and Φ parameters were determined for the 11 plug samples using the multistage triaxial test. It was observed that these parameters had the best correlation with

the effective porosity (PHIE), which is derived from the petrophysical evaluation (Fig. 3c). Therefore, the relationships obtained in Fig. 3c and d were used to estimate the C and Φ values in a continuous manner.

$$C = 233.35PHIE^2 - 95.31PHIE + 14.523 \tag{5}$$

$$\Phi = 672.49PHIE^2 - 339.81PHIE + 68.473 \tag{6}$$

In this study, the E_d was converted to E_s values using the Eq. 3. UCS was estimated continuously, using the Eq. 4. The C and Φ curves were estimated using the Eqs. 5 and 6, respectively.

Pore pressure

The Eaton equation (Eaton 1975) for estimating pore pressure, using petrophysical logs, is as follows:

$$P_{Pg} = S_V - (S_V - P_{PHyd}) \left(\frac{NCT}{DT} \right)^3 \tag{7}$$

Table 2 The results of uniaxial test on the 16 plug samples

Samples ID	Depth (m)	ρ (gr/cm ³)	Porosity (V/V)	Es (GPa)	UCS (MPa)
S1	3708.20	2.59	0.04	16.71	105.84
S2	3721.04	2.54	0.06	14.09	27.93
S4	3729.24	2.59	0.04	21.20	71.68
S5	3748.52	2.12	0.27	6.53	16.60
S6	3750.74	2.27	0.19	3.12	15.19
S7	3743.05	2.33	0.16	2.69	14.52
S9	3743.7	2.26	0.20	2.80	12.33
S13	3755.73	2.13	0.26	4.46	12.95
S15	3824.19	2.39	0.13	5.04	31.22
S16	3837.13	2.45	0.10	9.27	44.13
S19	3890.55	2.26	0.20	4.40	28.60
S21	3896.5	2.32	0.16	8.67	52.30
S22	3926.19	2.28	0.18	3.06	14.25
S23	3930.61	2.10	0.29	3.13	13.81
S25	3936.39	2.18	0.24	4.21	19.29
S28	3949.59	2.14	0.26	2.83	17.02

where P_{Pg} is pore pressure gradient, S_V is vertical stress magnitude, P_{PHyd} is hydrostatic pore pressure gradient, DT is slowness of compressional wave, and NCT is normal compaction trend of the sediments. Zhang (2011) modified Eaton’s equation for estimation of pore pressure as follows:

$$P_{Pg} = S_V - (S_V - P_{PHyd}) \left(\frac{DT_m + (DT_{ml} - DT_m)e^{-cZ}}{DT} \right)^3 \quad (8)$$

where DT_m is P wave slowness in shale lithology with zero porosity, DT_{ml} is P wave slowness in drilling mud, c is an experimental constant, and Z is the depth.

In this study, it was observed that by considering $c = 0.0005$ and the coefficient power equal to 0.44, a good correlation between MDT points and estimated pore pressure curve will be obtained.

Table 3 The results of multistage triaxial tests on the 11 plug samples

Samples ID	Depth (m)	ρ (gr/cm ³)	Porosity (V/V)	C (MPa)	Φ (deg)
S3	3729.17	2.59	0.04	10.75	53.28
S8	3743.50	2.30	0.18	4.19	29.77
S10	3744.06	2.14	0.26	4.67	23.19
S11	3749.25	2.15	0.26	3.56	31.00
S12	3755.32	2.07	0.31	5.56	22.41
S14	3786.25	2.21	0.22	4.05	30.60
S17	3872.73	2.35	0.15	5.50	31.14
S18	3890.48	2.31	0.17	6.37	28.65
S20	3896.33	2.32	0.16	4.92	44.02
S26	3936.46	2.29	0.18	6.50	36.61
S27	3949.52	2.08	0.30	7.63	29.90

Estimation of the principal stresses

The magnitude of vertical stress (S_V) is determined using the overburden weight (Jaeger and Cook 1979):

$$S_V = \int_0^z \rho(z)g \, dz \approx \bar{\rho}gz \quad (9)$$

where z is depth, $\rho(z)$ is rock density as a function of depth, g is Earth’s gravity acceleration, and $\bar{\rho}$ is overburden average density.

The poroelastic equations are used to estimate the maximum (S_{Hmax}) and minimum (S_{Hmin}) horizontal stresses (Fjaer et al. 1992):

$$S_{Hmin} = \frac{\nu}{(1-\nu)}(S_V - \alpha PP) + \alpha PP + \frac{E_S}{(1-\nu^2)} \epsilon_x + \frac{\nu \times E_S}{(1-\nu^2)} \epsilon_y \quad (10)$$

$$S_{Hmax} = \frac{\nu}{(1-\nu)}(S_V - \alpha PP) + \alpha PP + \frac{E_S}{(1-\nu^2)} \epsilon_y + \frac{\nu \times E_S}{(1-\nu^2)} \epsilon_x \quad (11)$$

where ν is Poisson’s ratio, S_V is vertical stress, α is Biot’s coefficient (in the absence of data, is conventionally considered as 1), PP is pore pressure, and E_S is static Young’s modulus. Moreover, the tectonic strain on x (ϵ_x) and y (ϵ_y) axes are determined by the following equations (Kidambi and Kumar 2016):

$$\epsilon_x = \frac{S_V \times \nu}{E_S} \left(\frac{1}{1-\nu} - 1 \right) \quad (12)$$

$$\epsilon_y = \frac{S_V \times \nu}{E_S} \left(1 - \frac{\nu^2}{1-\nu} \right) \quad (13)$$

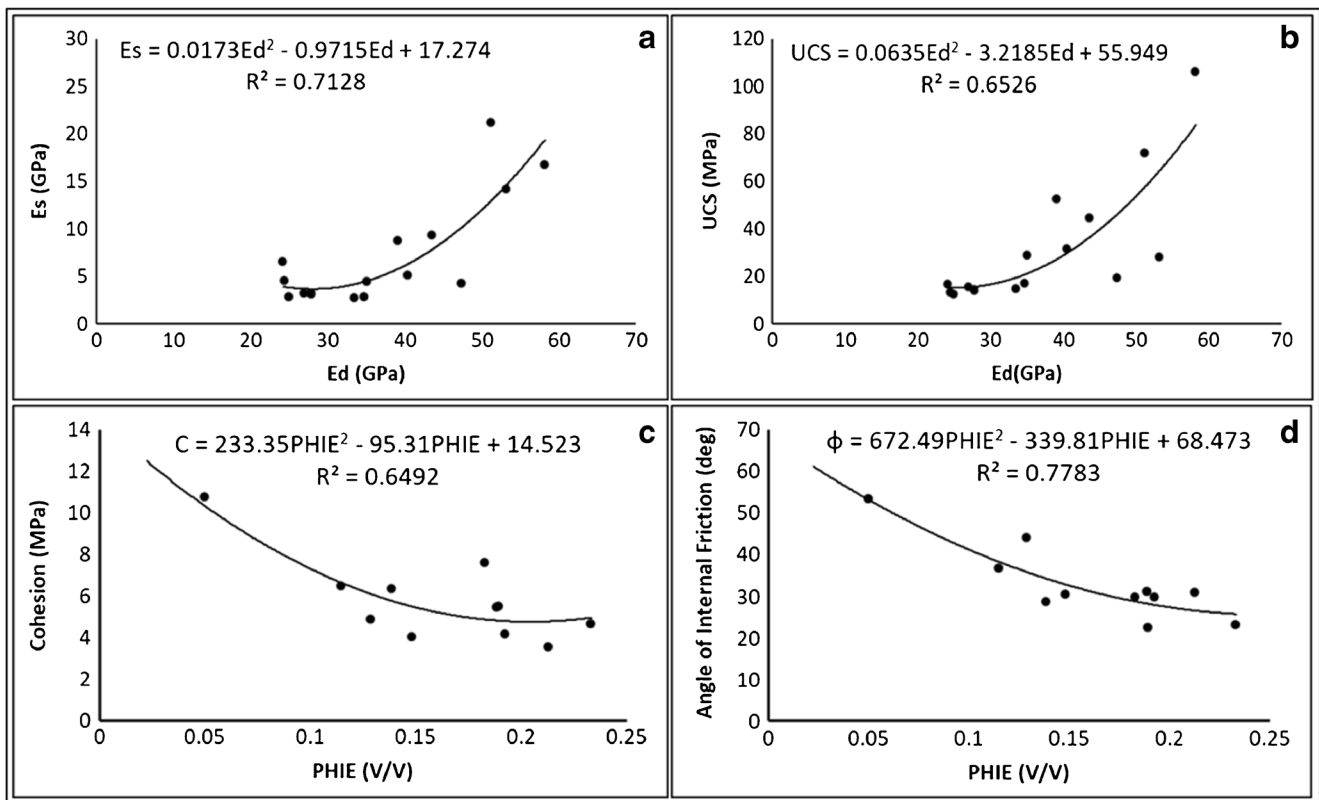


Fig. 3 a Static Young’s modulus vs. dynamic Young’s modulus. b UCS vs. dynamic Young’s modulus. c Cohesion vs. effective porosity. d Angle of internal friction vs. effective porosity

Wellbore stability

Generally, if the drilling fluid pressure is lower than the break-out pressure, shear failure occurs. On the other hand, if the pressure of the drilling mud reaches the minimum principal stress, mud loss happens. One of the main applications of geomechanical model is to determine the optimum drilling mud weight.

The distance between the pore pressure and minimum principal stress is called safe mud window, in which case we may have breakouts. Also, the distance between the breakout and breakdown pressures is called stable mud window (Nabaei

et al. 2011). At best, the weight of the drilling mud should be determined in such a way to avoid the formation of bore-hole breakouts and mud loss (safe/stable mud window).

Wellbore wall stresses

The stresses affecting the wellbore wall can be determined using Kirsch equations (Zoback 2010). Based on these equations, effective radial (σ_r), tangential (σ_θ), and axial (σ_z) stresses are calculated around a vertical well with radius R as follows:

Table 4 Breakout P_w pressure according to Mohr-Coulomb failure criterion (Al-Ajmi and Zimmerman, 2006)

Case	Stress relationship	If $P_w \leq P_{wb}$ borehole failure occurs
1	$\sigma_z \geq \sigma \geq \sigma_r$	$P_{wb} = (B - c)/q$
2	$\sigma \geq \sigma_z \geq \sigma_r$	$P_{wb} = (A - c)/(1 + q)$
3	$\sigma \geq \sigma_r \geq \sigma_z$	$P_{wb} = A - c - qB$

$A = 3S_{Hmax} - S_{hmin}$
 $B = S_V + 2\nu(S_{Hmax} - S_{hmin})$
 $c = UCS + PP(q - 1)$

Table 5 Fracture P_w pressure according to Mohr-Coulomb failure criterion (Al-Ajmi and Zimmerman, 2006)

Case	Stress relationship	If $P_w \geq P_{wf}$ borehole failure occurs
1	$\sigma_r \geq \sigma \geq \sigma_z$	$P_{wf} = c + qE$
2	$\sigma_r \geq \sigma_z \geq \sigma$	$P_{wf} = (c + qD)/(1 + q)$
3	$\sigma_z \geq \sigma_r \geq \sigma$	$P_{wf} = (c - E)/q + D$

$E = 3S_{hmin} - S_{Hmax}$
 $D = S_V - 2\nu(S_{Hmax} - S_{hmin})$

Table 6 Breakout P_w pressure according to Mogi-Coulomb failure criterion (Al-Ajmi and Zimmerman, 2006)

Case	Stress relationship	If $P_w \leq P_{wb}$ borehole failure occurs
1	$\sigma_z \geq \sigma \geq \sigma_r$	$P_{wb} = \frac{1}{6-2b^2} \left[(3A + 2b'K) - \sqrt{H + 12(K^2 + b'AK)} \right]$
2	$\sigma \geq \sigma_z \geq \sigma_r$	$P_{wb} = \frac{A}{2} - \frac{1}{6} \sqrt{12[a' + b'(A-2PP)]^2 - 3(A-2B)^2}$
3	$\sigma \geq \sigma_r \geq \sigma_z$	$P_{wb} = \frac{1}{6-2b^2} \left[(3A + 2b'G) - \sqrt{H + 12(G^2 + b'AG)} \right]$

$A = 3S_{Hmax} - S_{hmin}$
 $B = S_V + 2\nu(S_{Hmax} - S_{hmin})$
 $K = a' + b'(B - 2PP)$
 $H = A^2(4b^2 - 3) + (B^2 - AB)(4b^2 - 12)$
 $G = K + b'A$

$$\sigma_r = \frac{1}{2}(S_{Hmax} + S_{hmin} - 2PP) \left(1 - \frac{R^2}{r^2} \right) + \frac{1}{2}(S_{Hmax} - S_{hmin}) \times \left(1 - \frac{4R^2}{r^2} + \frac{3R^4}{r^4} \right) \cos 2\theta + \frac{PPR^2}{r^2} \quad (14)$$

$$\sigma_\theta = \frac{1}{2}(S_{Hmax} + S_{hmin} - 2PP) \left(1 + \frac{R^2}{r^2} \right) - \frac{1}{2}(S_{Hmax} - S_{hmin}) \times \left(1 + \frac{3R^4}{r^4} \right) \cos 2\theta - \frac{PPR^2}{r^2} - \sigma^{\Delta T} \quad (15)$$

$$\sigma_z = S_V - 2\nu(S_{Hmax} - S_{hmin}) \cos 2\theta - PP - \sigma^{\Delta T} \quad (16)$$

where θ is the angle from the S_{Hmax} direction azimuth, r is desired distance from wellbore wall, ΔP is the difference between the drilling mud pressure and the pore pressure (PP), and $\sigma^{\Delta T}$ is the thermal stress caused by the temperature difference between the drilling mud and the formation. In case of $r = R$ (in the wellbore wall), the σ_θ and σ_r on the wellbore wall are:

$$\sigma_\theta = S_{hmin} + S_{Hmax} - 2(S_{Hmax} - S_{hmin}) \cos 2\theta - 2PP - \Delta P - \sigma^{\Delta T} \quad (17)$$

$$\sigma_r = \Delta P \quad (18)$$

In this study, the stresses around the wellbore were calculated using Eqs. 16 to 18.

Mohr–Coulomb failure criterion

After calculating the stresses and mechanical properties of the rocks, stability of wells can be investigated using failure criteria. According to Mohr–Coulomb criterion, normal stress (S_n) and shear stress (τ) at the failure can be expressed by (Mohr 1900):

$$\tau = C + \mu S_n \quad (19)$$

where C and μ are cohesion and coefficient of internal friction, respectively. Also, the linearized form of the Mohr–Coulomb criterion is relating the maximum (S_1) and minimum (S_3) principal stresses (Al-Ajmi and Zimmerman 2006):

$$S_1 = UCS + qS_3 \quad (20)$$

where:

$$q = \tan^2 + \left(\frac{\pi}{4} + \frac{\Phi}{2} \right) \quad (21)$$

Table 7 Fracture P_w pressure according to Mogi-Coulomb failure criterion (Al-Ajmi and Zimmerman, 2006)

Case	Stress Relationship	If $P_w \geq P_{wf}$ borehole failure occurs
1	$\sigma_r \geq \sigma \geq \sigma_z$	$P_{wf} = \frac{1}{6-2b^2} \left[(3D + 2b'N) - \sqrt{J + 12(N^2 + b'DN)} \right]$
2	$\sigma_r \geq \sigma_z \geq \sigma$	$P_{wf} = \frac{D}{2} - \frac{1}{6} \sqrt{12[a' + b'(D-2PP)]^2 - 3(D-2E)^2}$
3	$\sigma_z \geq \sigma_r \geq \sigma$	$P_{wf} = \frac{1}{6-2b^2} \left[(3D + 2b'M) - \sqrt{J + 12(M^2 + b'DM)} \right]$

$D = S_V - 2\nu(S_{Hmax} - S_{hmin})$
 $N = a' + b'(E - 2PP)$
 $J = D^2(4b^2 - 3) + (E^2 - DE)(4b^2 - 12)$
 $M = N + b'D$

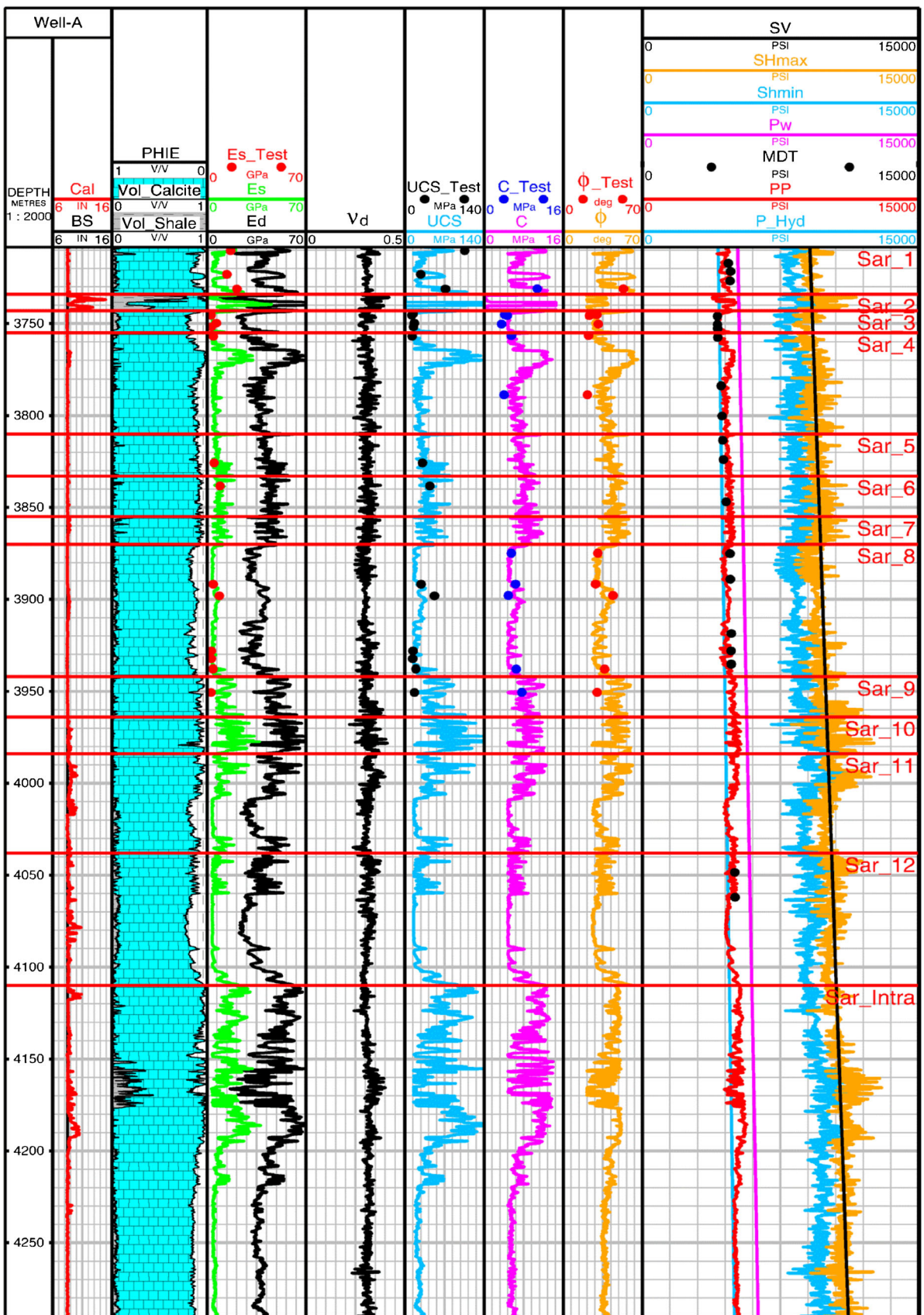


Fig. 4 The 1D geomechanical model of well-A. The S_{Hmax} is approximately equal to the S_v , which generally shows a strike-slip normal stress state. Moreover, the pore pressure is close to hydrostatic pore pressure

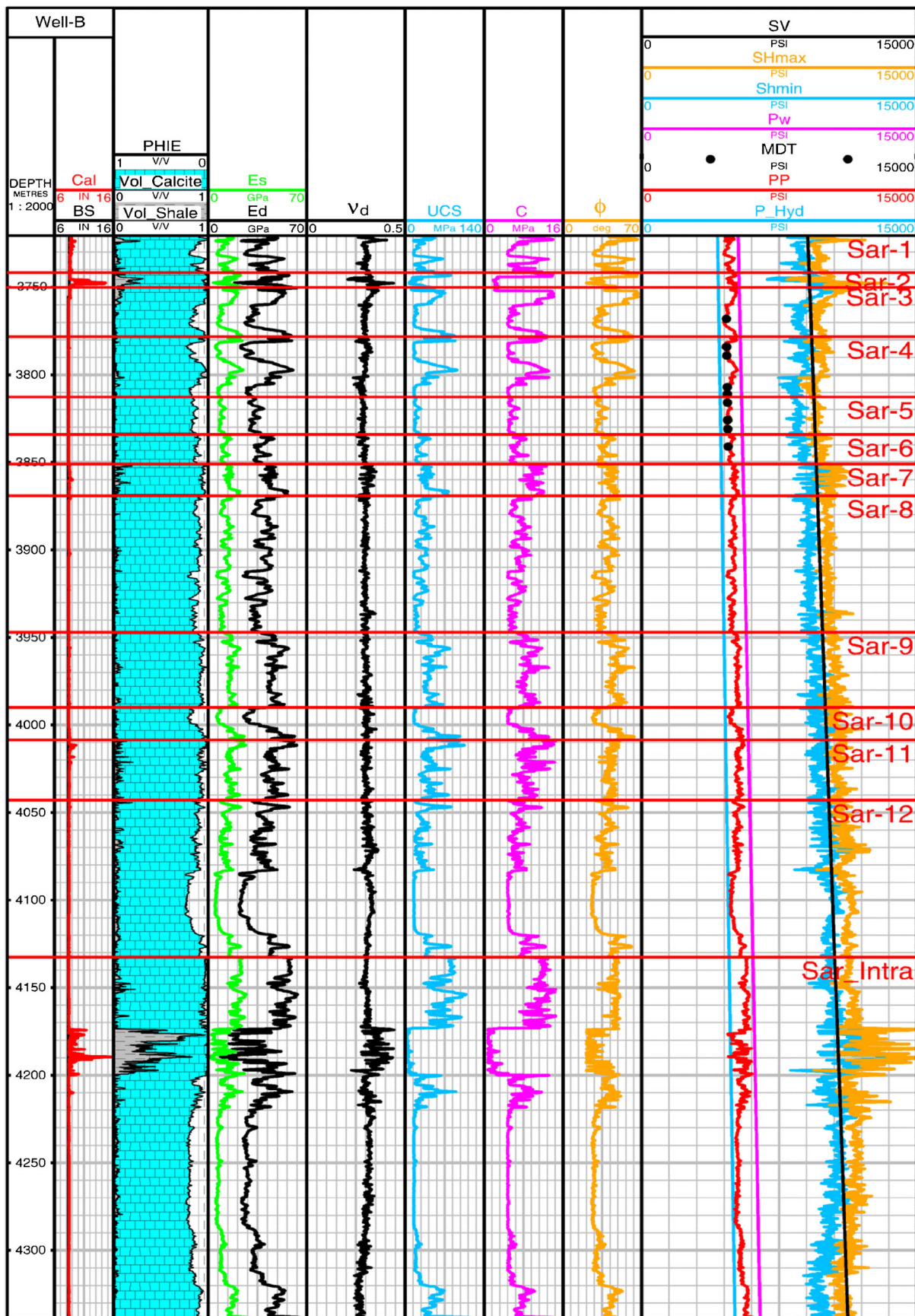


Fig. 5 The 1D geomechanical model of well-B. The stress state is generally strike-slip, and pore pressure is higher than well-A

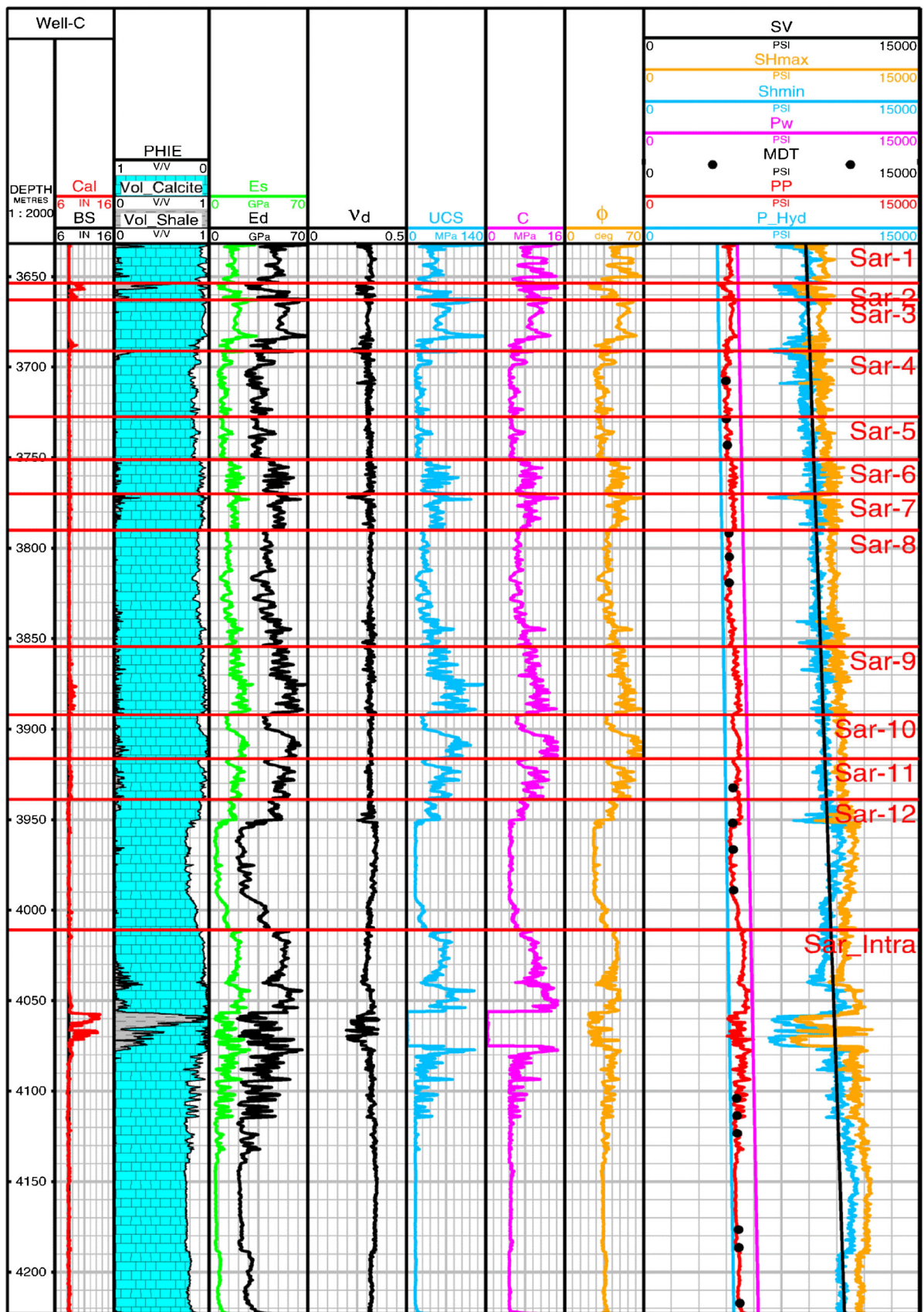


Fig. 6 The 1D geomechanical model of well-C. The stress state is generally strike-slip reverse, but horizontal stresses from 4053 to 4072 m are very low, which could be related to the shale lithology

Table 8 Average values of geomechanical parameters in the studied wells

Parameter	Well-A	Well-B	Well-C
E_d (GPa)	40.27	39.94	40.84
E_s (GPa)	9.55	13.16	13.78
ν_d	0.31	0.30	0.31
UCS (MPa)	40.42	34.57	39.02
C (MPa)	7.71	7.30	7.32
Φ (deg)	39.71	38.38	39.82
PP (psi)	4885.73	5195.90	5006.90
S_{hmin} (psi)	9063.10	9804.85	9896.76
S_{Hmax} (psi)	10,191.13	10,823.31	10,817.46
S_V (psi)	10,219.67	10,225.300	9968.89

Regarding to effective stress concept, the Mohr–Coulomb criterion can be rewritten as:

$$S_1 = c + qS_3 \tag{22}$$

where

$$c = UCS + PP(q-1) \tag{23}$$

The breakout pressure and fracture pressure from Mohr–Coulomb criterion are shown in Tables 4 and 5. In these tables, P_w is actual drilling mud pressure, P_{wb} is drilling mud pressure which causes borehole breakouts, and P_{wf} is drilling mud pressure which causes induced fractures.

Mogi–Coulomb failure criterion

It was concluded by Mogi (1971) that the mean normal stress which opposes the creation of the fracture plane will be $S_{m,2}$, and therefore, a new failure criterion was suggested:

$$\tau_{oct} = f(S_{m,2}) \tag{24}$$

where $S_{m,2}$ and τ_{oct} are the effective mean stress and octahedral shear stress, respectively. The $S_{m,2}$ and octahedral shear stress are defined as follows:

$$S_{m,2} = \frac{S_1 + S_3}{2} \tag{25}$$

$$\tau_{oct} = \frac{1}{3} \sqrt{(S_1 - S_2)^2 + (S_2 - S_3)^2 + (S_3 - S_1)^2} \tag{26}$$

Al-Ajmi and Zimmerman (2006) used Mogi–Coulomb criterion and suggested a function to relate parameters of this criterion to the Mohr–Coulomb strength parameters, C and Φ . $S_{m,2}$ and τ_{oct} are the effective mean stress and octahedral shear stress which are formulated as follows (Al-Ajmi and Zimmerman 2006):

$$\tau_{oct} = a + bS_{m,2} \tag{27}$$

where:

$$a = \frac{2\sqrt{2}}{3} C \cos\Phi \tag{28}$$

$$b = \frac{2\sqrt{2}}{3} C \sin\Phi \tag{29}$$

There are determined invariants related to the stress tensor, which their values are independent of the chosen coordinate system. With regard to the first and second stress invariants, I_1 and I_2 will be:

$$I_1 = S_1 + S_2 + S_3 \tag{30}$$

$$I_2 = S_1S_2 + S_2S_3 + S_3S_1 \tag{31}$$

where S_1 , S_2 , and S_3 are maximum, intermediate, and minimum principal stresses, respectively. Using the effective stress concept (Al-Ajmi and Zimmerman 2006):

$$\sqrt{(I_1^2 - 3I_2)} = a' + b'(I_1 - S_2 - 2PP) \tag{32}$$

where

$$a' = 2C \cos\Phi \tag{33}$$

$$b' = \sin\Phi \tag{34}$$

The borehole breakout and fracture pressures from Mogi–Coulomb criterion are shown in Tables 6 and 7, respectively.

Results

Geomechanical models

Figures 4, 5, and 6 show the 1D geomechanical models of the three studied wells. In these figures, the tracks from left to right are depth, caliper-bit size, lithology, dynamic and static Young’s modulus, dynamic Poisson’s ratio, UCS, cohesion, angle of internal friction and stresses/pressures.

In Fig. 4 (well-A), generally, the S_{Hmax} is approximately equal to the S_V , and these two stresses are larger than S_{hmin} , indicating that the stress regime in this well for the Sarvak reservoir is strike-slip normal ($S_{Hmax} = S_V > S_{hmin}$). However, in some zones (e.g., Sar-4 to Sar-7), the S_{Hmax} is higher than the S_V , which represents a strike-slip stress regime.

In the Sarvak Formation of well-B, S_{Hmax} is generally greater than S_V , and S_{hmin} is less than S_V (Fig. 5). Therefore, the stress state is strike-slip ($S_{Hmax} > S_V > S_{hmin}$). Generally, the pore pressure of this well is larger than well-A. The pore pressure of this well is partly separated from the hydrostatic pore pressure (Fig. 5). In well-C, S_V and S_{hmin} are mostly equal, and both are smaller than S_{Hmax} (Fig 6), which indicates a strike-slip reverse stress state ($S_{Hmax} > S_V = S_{hmin}$).

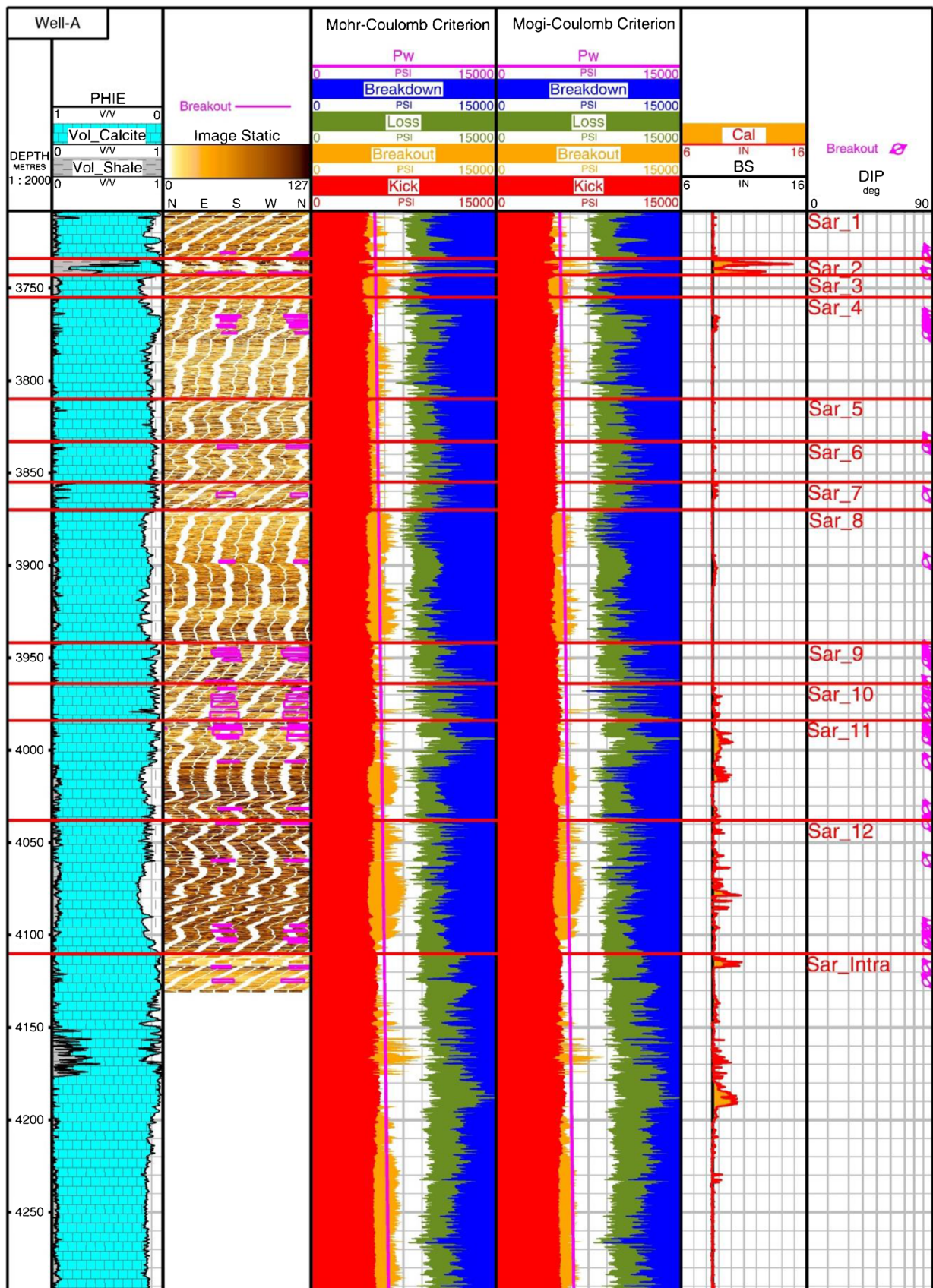


Fig. 7 The wellbore stability analysis for well-A. At most depths, the mud pressure line (P_w) situated in the breakout zone (orange color), but Mogi-Coulomb criterion breakout pressure is more acceptable regarding to the recognized breakouts

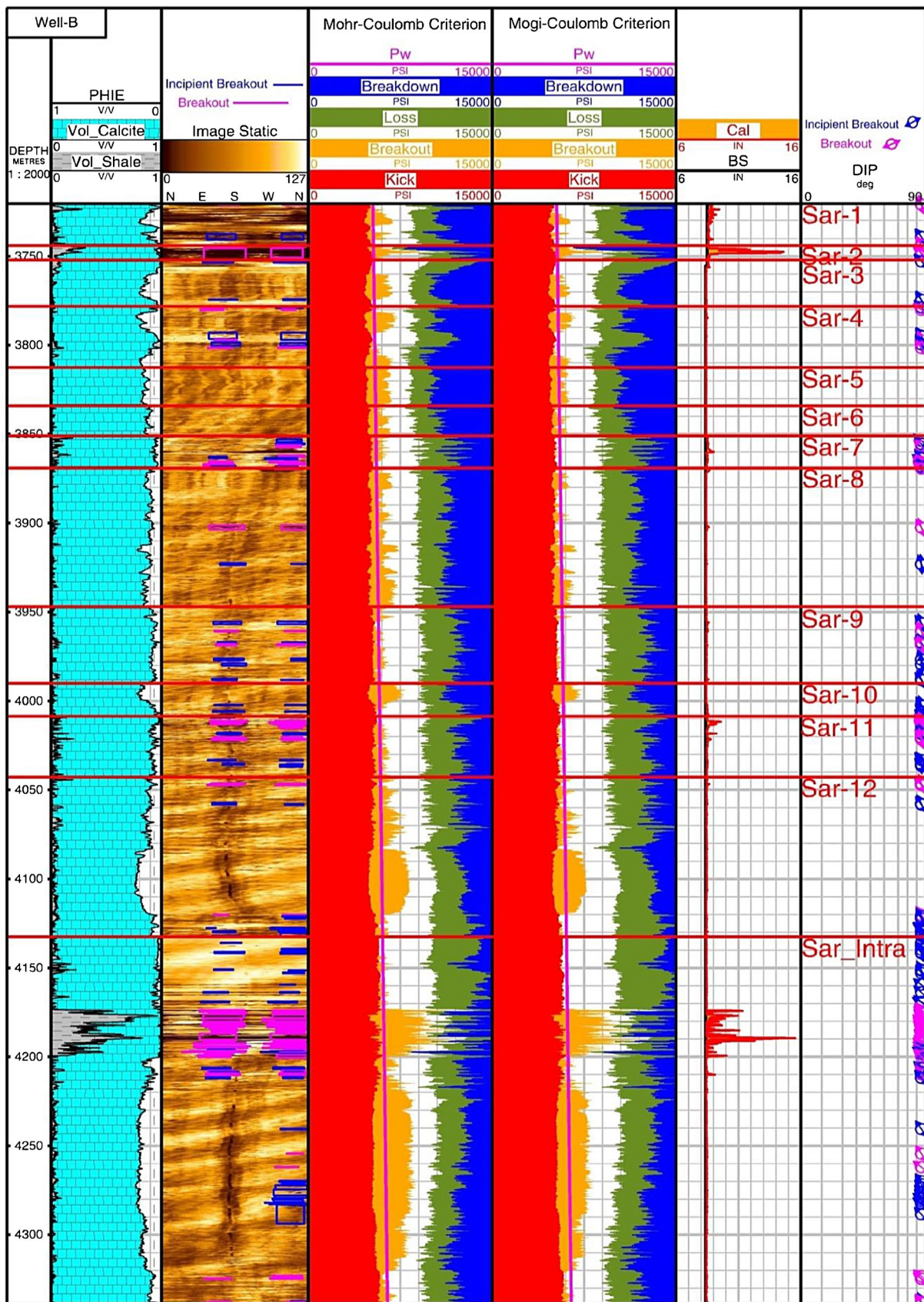


Fig. 8 The wellbore stability analysis for well-B. Like well-A, breakout pressure is overestimated by Mohr-Coulomb criterion, but major breakout part in Sar_Intra well-recognized by the both failure criteria

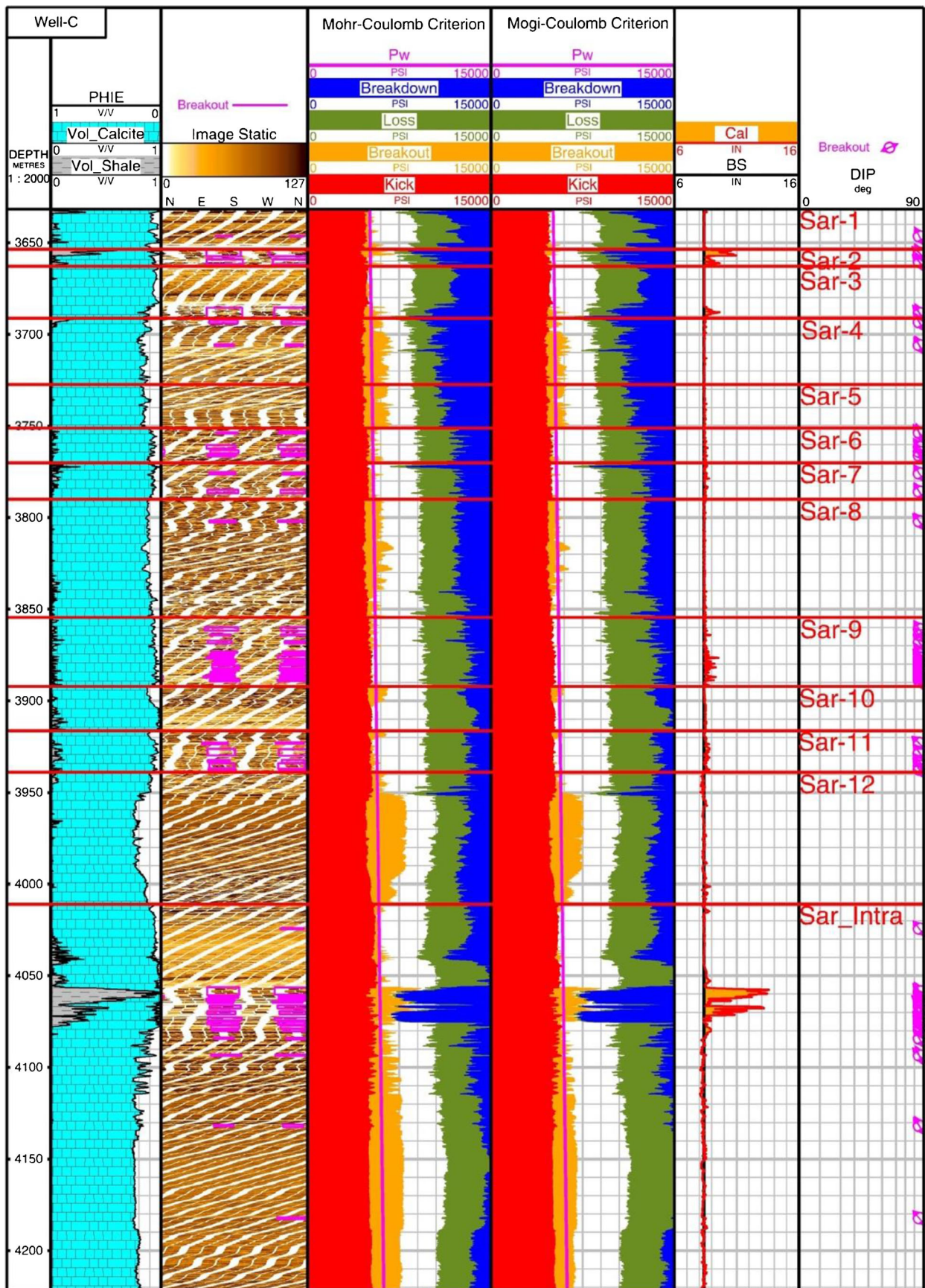


Fig. 9 The wellbore stability analysis for well-C. In the depth 4053 to 4072 m, the upper limit of mud weight is very low

Table 9 Drilling mud weight and mud loss volume in the studied wells

Well	Mud Weight (pcf)	Mud Loss (bbl/h)
A	82	0.5 to 6
B	85	1 to 5
C	85	2 to 6

Table 8 shows the statistical parameters of principal stresses and mechanical properties of the rocks in three studied wells (based on the 1D models). In all wells, the E_d , ν_d , C , and Φ have similar average values. Moreover, based on the average values of the stresses, the in situ stress regimes in well-A, well-B, and well-C are strike-slip normal, strike-slip, and strike-slip reverse, respectively. However, the average pore pressure in well-B and well-C is greater than well-A.

Wellbore stability analysis

In the studied wells, the relationship among the wellbore wall stresses is $\sigma_\theta \geq \sigma_z \geq \sigma_r$. Hence, the second equations in Tables 4 and 6 were used to calculate the breakout pressure. The usual condition of wellbore wall stresses relationship to create induced fractures is $\sigma_r \geq \sigma_z \geq \sigma_\theta$ (Al-Ajmi and Zimmerman 2006; Maleki et al. 2014). Therefore, the second equations in Tables 5 and 7 were used for the fractures pressure calculation in the studied wells.

In Figs. 7, 8 and 9, the tracks from left to right are showing depth, lithology, image log (static image), wellbore stability analysis using Mohr-Coulomb criterion, wellbore stability analysis using Mogi-Coulomb criterion, caliper-bit size and the recognized borehole breakouts based on the image logs. In wellbore stability analysis, the tracks with red, orange, green, and blue colors indicate the kick, breakouts, loss, and breakdown limits, respectively. Also, the actual mud pressure (P_w) is shown with a purple line.

In all three wells, the pressure of the selected drilling mud (P_w) is close to the pore pressure (kick pressure). Table 9 shows the drilling mud weight and the volume of mud loss

in the Sarvak Formation of the studied wells. Based on Table 9, mud loss is very low and can be considered as seepage for the wells (Figs. 7, 8 and 9).

The Mohr-Coulomb breakout pressures are higher than Mogi-Coulomb pressures (Figs. 7, 8 and 9). However, considering the borehole failures (caliper-bit size and image logs), it seems that Mogi-Coulomb breakout pressure is more compatible with the wellbore failures. In well-B, from 4175 to 4200-m depth, there is a major breakout zone which is well-recognized by both failure criteria (Fig. 8). In well-C, from 4053 to 4072-m depth, there is a breakout interval; and also the minimum principal stress is very low in this zone (Fig. 9).

The mud weight windows were determined for the three wells using geomechanical models and failure criteria (Table 10). According to the analysis, in all the wells, the Mohr-Coulomb breakout pressures are higher than Mogi-Coulomb breakout pressure (Table 10).

The orientations of the horizontal stresses in the studied wells are shown in Table 11. The S_{Hmax} orientation in all the three wells is NE-SW. In this study, S_{Hmin} and S_{Hmax} directions were determined using a large number of breakout observations in the image logs. The formations which used to identify horizontal stresses direction are mentioned in Table 11. In these formations, the horizontal stresses direction is uniform. Based on the quality ranking system for stress indicators (Zoback 2010), the quality of these directions are considered as "A."

The direction of horizontal stresses has a great influence on the stability of the deviated wells. In directional wells, the direction where the stress difference on the wellbore wall is smaller would be more stable.

The effect of horizontal stress orientation on the stability of wells was evaluated for the three wells (Fig. 10). Near the well-A, due to the strike-slip normal stress regime, higher mud weight is needed to prevent borehole breakouts in vertical and NE-SW-directed wells. In this region, the most stable drilling is to the S_{Hmin} direction, i.e., NW-SE (Fig. 10). Near the well-B, as a strike-slip stress state, the most stable directions are toward N10 °E and N80 °W (Fig. 10). Near the well-C, as a strike-slip reverse stress state, the most stable direction is toward S_{Hmax} , i.e., NE-SW (Fig. 10).

Table 10 Mud weight windows in the studied wells

Well	Safe mud window (pcf)	Stable mud window (pcf)	Safe/stable mud window (pcf)
A	78.6–117.3	Mohr-Coulomb	99.6–124.2
		Mogi-Coulomb	89.7–120.1
B	82.2–114.9	Mohr-Coulomb	106.5–127.4
		Mogi-Coulomb	97.8–123.3
C	79.2–97.4	Mohr-Coulomb	103.8–99.2
		Mogi-Coulomb	92.5–100.3

Table 11 The horizontal stress orientations in the studied wells

Well	Formations	Image log length (m)	Breakout count	Breakout total length(m)	Standard deviation of breakouts direction	S _{hmin} orientation (mean value)	S _{Hmax} orientation (mean value)
A	Sarvak to Gurpi	781	156	151.75	7.31°	N29 °W	N61 °E
B	Dariyan to Gurpi	1376	592	488.96	9.66°	N39.5 °W	N50.5 °E
C	Fahliyan to Gurpi	1876	460	915.07	7.38°	N31.5 °W	N58.5 °E

Discussion

Apparently, porosity has a great influence on Young’s modulus and UCS. Same as E_s and UCS, porosity also has a significant effect on the C and Φ. Also, the reduction of the angle of internal friction with porosity increase for sandstone samples has also been reported (Chang et al. 2006). The mean of E_s is equal to 7.01 GPa, while the mean of E_d is 40.27 GPa. Therefore, there is a large difference between the values of the static and dynamic Young’s modulus in the Sarvak reservoir.

The pore pressure gradient of Sar-1 is relatively higher than the other zones in well-A. Sar-1 situated between two shaly layers (i.e., Lafan formation and Sar-2), in this condition, the vertical displacement of the fluids in Sar-1 is restricted and pore pressure increased. Although Sar-3 and Sar-8 which are considered as good reservoir zones (due to high porosity and low water saturation), have a relatively low pore pressure which is close to the hydrostatic pore pressure (Fig. 4).

Generally, in all of the three wells, the pore pressure of Sarvak Formation is close to the hydrostatic pore pressure.

Therefore, in the future, production will not be possible without improved/enhanced oil recovery technologies. Also, if the pore pressure is reduced below the hydrostatic pressure, a lighter mud weight is needed for Sarvak reservoir, and a new casing may be needed for this reservoir.

The difference between pore pressure and minimum principal stress of the studied wells is often relatively high. Therefore, the probability of induced fracturing in the Sarvak Formation is very low; this is in line with the fact that no induced fractures could be detected in the image logs. Also, according to Figs. 7, 8 and 9, it is clear that the difference between the mud pressures and the estimated minimum stresses in all studied wells is high.

The Mohr-Coulomb mud weight results are more conservative than Mogi–Coulomb criterion. For instance, in the lower part of the Sar_intra zone of well-A (Fig. 7), the wellbore wall is in stable condition regarding to Mogi–Coulomb criterion, and caliper bit-size track confirms this, but Mohr-Coulomb criterion indicates that such breakouts should happen in this interval (Fig. 7).

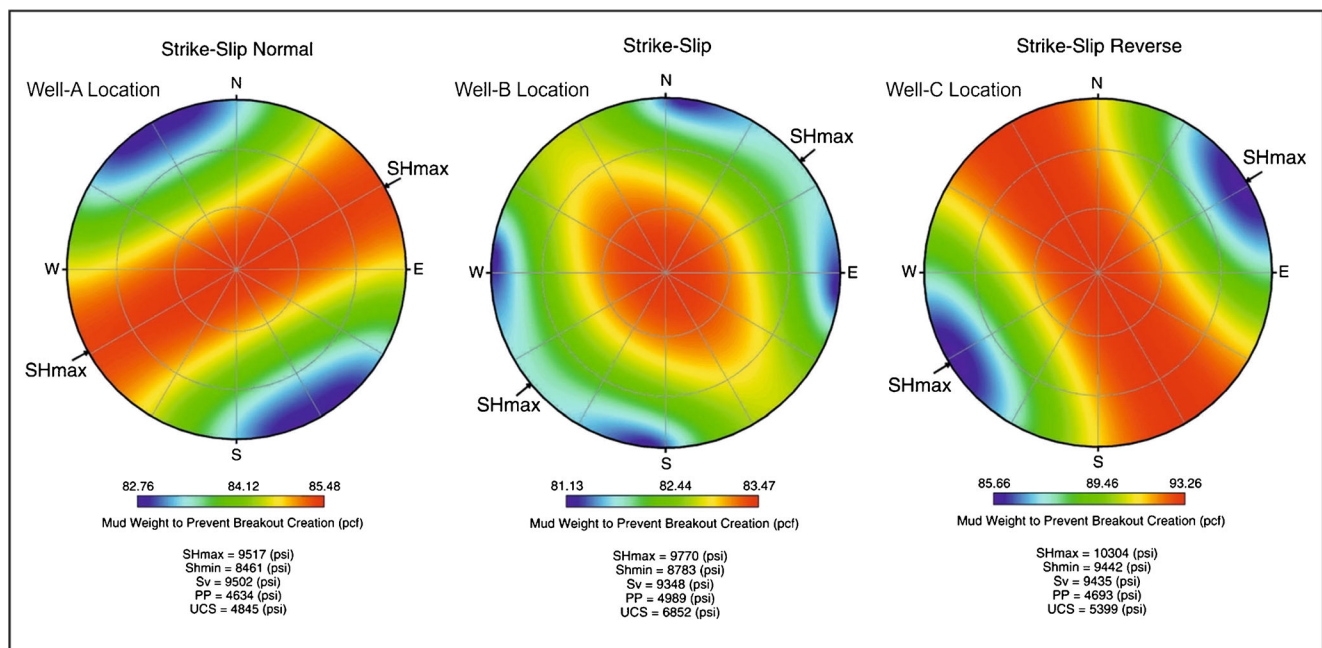


Fig. 10 Analysis of wellbore stability in different drilling directions. Note the minimum mud weight required to prevent borehole breakouts in different drilling directions

In the well-C, Mohr-Coulomb breakout pressure gradient is higher than the fracture pressure gradient, because the breakout pressure is overestimated at 3950 to 4000-m and 4053 to 4072-m depth intervals (Fig. 9), and the fracture pressure is very low. Hence, based on the Mohr-Coulomb criterion, the mud pressure gradient that avoids breakouts at 3950 to 4000 m causes fracturing at the 4053 to 4072-m depth. Also, in this interval, the safe mud weight window is very narrow, due to the presence of a shale layer. Minimum horizontal stress and tensile strength of this zone are low; so there is a risk of total mud loss in this interval.

Conclusion

In this study, 1D geomechanical models were constructed for three wells in the north, center, and south parts of an oil field in the Abadan Plain. In the north well, E_S and UCS were determined using uniaxial test. Also, C and Φ were measured using triaxial tests. Furthermore, several relationships were presented for converting E_d to E_S and estimating UCS, C , and Φ based on the geomechanical tests and well logs integration.

The pore pressure in the Sarvak reservoir of the studied oil field is low and close to the hydrostatic state. Therefore, for the future production, enhanced oil recovery programs should be considered. Also, with decreasing pore pressure, the Sarvak Formation may need a different mud weight for drilling and subsequently a new casing.

According to the 1D geomechanical models, the in situ stress regimes in the north, center, and south wells are strike-slip normal, strike-slip, and strike-slip reverse, respectively. Based on the picked borehole breakouts, the S_{Hmax} orientations in the three wells are toward NE-SW. In all wells, the failure was of breakout type, and induced fracture type was not observed. By comparing the wellbore stability models with the failures detected using image logs and caliper bit-size, it was found that the Mogi-Coulomb criterion performs a better stability model than Mohr-Coulomb criterion.

According to the in situ stress magnitudes and orientation of horizontal stresses, it is concluded that in the north, center, and south wells, the more stable drilling directions are NW-SE, $N10^\circ E$ and $N80^\circ W$, and NE-SW, respectively.

This paper is a part of an ongoing research, which includes the development of the 3-D geomechanical model; however, in current manuscript, the results of the application of 1D geomechanical for wellbore stability purposes are addressed. The assumptions for developing the 1D geomechanical model were thoroughly outlined in the paper.

Acknowledgements The authors appreciate Research Institute of Petroleum Industry (RIPI) for the publishing permission and financial support. Appreciation is given to SeaLand Engineering and Well Services (SLD) for its supports.

References

- Abdollahie-Fard I, Braathen A, Mokhtari M, Alavi SA (2006) Interaction of the Zagros fold-thrust belt and the Arabian-type, deep-seated folds in the Abadan Plain and the Dezful Embayment, SW Iran. *Pet Geosci* 12:347–362
- Aghajanpour A, Fallahzadeh SH, Khatibi S, Hossain MM, Kadkhodaie A (2017) Full waveform acoustic data as an aid in reducing uncertainty of mud window design in the absence of leak-off test. *J Nat Gas Sci Engin* 45:786–796
- Akhtarmanesh S, Shahrabi MA, Atashnezhad A (2013) Improvement of wellbore stability in shale using nanoparticles. *J Pet Sci Eng* 112: 290–295
- Al-Ajmi AM, Zimmerman RW (2006) Stability analysis of vertical boreholes using the Mogi-Coulomb failure criterion. *Int J Rock Mech Min Sci* 43(8):1200–1211
- Ali AHA, Brown T, Delgado R, Lee D, Plumb D, Smimov N, Marsden R, Prado-Velarde E, Ramsey L, Spooner D, Stone T (2003) Watching rocks change mechanical earth modeling. *Oilfield Rev* 15(1):22–39
- Assadi A, Honarmand J, Moallemi SA, Abdollahie-Fard I (2016) Depositional environments and sequence stratigraphy of the Sarvak formation in an oil field in the Abadan Plain, SW Iran. *Facies* 62(4):1–22
- Awal MR, Khan MS, Mohiuddin MA, Abdulraheem A, Azeemuddin M (2001) A new approach to borehole trajectory optimisation for increased hole stability. In SPE Middle East Oil Show, Society of Petroleum Engineers
- Azadpour M, Manaman NS, Kadkhodaie-Ilkhchi A, Sedghipour MR (2015) Pore pressure prediction and modeling using well-logging data in one of the gas fields in south of Iran. *J Pet Sci Eng* 128:15–23
- Chang C, Zoback MD, Khaksar A (2006) Empirical relations between rock strength and physical properties in sedimentary rocks. *J Pet Sci Eng* 51(3):223–237
- Chen G, Chenevert ME, Sharma MM, Yu M (2003) A study of wellbore stability in shales including poroelastic, chemical, and thermal effects. *J Pet Sci Eng* 38(3–4):167–176
- Darvish H, Nouri-Taleghani M, Shokrollahi A, Tatar A (2015) Geomechanical modeling and selection of suitable layer for hydraulic fracturing operation in an oil reservoir (south west of Iran). *J Afr Earth Sci* 111:409–420
- Eaton, B.A., 1975. The equation for geopressure prediction from well logs. Fall meeting of the Society of Petroleum Engineers of AIME, Dallas, Texas
- Ezati M, Azizzadeh M, Riahi MA, Fattahpour V, Honarmand J (2018) Characterization of micro-fractures in carbonate Sarvak reservoir, using petrophysical and geological data, SW Iran. *J Pet Sci Eng* 170:675–695
- Ezati M, Azizzadeh M, Riahi MA, Fattahpour V, Honarmand J (2019b) Application of DSI log in geomechanical and petrophysical evaluation of carbonate reservoirs: a case study in one of the SW Iranian oil fields. *J Petroleum Res* 29:37–50
- Ezati M, Olfati H, Khadem M, Yazdanipour MR, Mohammad A (2019a) Petrophysical Evaluation of a Severely Heterogeneous Carbonate Reservoir; Electrical Image Logs Usage in Porosity Estimation. *Open J Geol* 9(3)
- Ezati M, Soleimani B, Moazeni MS (2014) Fracture and horizontal stress analysis of Dalan formation using FMI image log in one of Southwestern Iranian oil wells. *J Tethys* 2(1):001–008

- Fattahpour V, Pirayehgar A, Dusseault MB, Mehrgini B (2012) Building a mechanical earth model: a reservoir in Southwest Iran. In: In 46th US rock mechanics/Geomechanics symposium. American Rock Mechanics Association
- Fjaer E, Holt RM, Hordrud P, Raaen AM, Risnes R (2008) Petroleum related rock mechanic. *Developments in Petroleum Science*. Elsevier, 491p
- Fjaer E, Horsrud P, Raaen AM, Risnes R, Holt RM (1992) Petroleum related rock mechanics, vol 33. Elsevier, Berlin, 338p
- Ghafoori M, Rastegarnia A, Lashkaripour GR (2018) Estimation of static parameters based on dynamical and physical properties in limestone rocks. *J Afr Earth Sci* 137:22–31
- Haghi AH, Kharrat R, Asef MR, Rezazadegan H (2013) Present-day stress of the central Persian Gulf: implications for drilling and well performance. *Tectonophysics* 608:1429–1441
- Hui Z, Deli G (2005) Review on drill bit selection methods. *Oil Drill Prod Technol* 27(4):1–4
- Jaeger JC, Cook NG (1979) *Fundamentals of rock mechanics*. Barnes and Noble, Methuen, London, New York, 593p
- Jaeger JC, Cook NG, Zimmerman R (2009) *Fundamentals of rock mechanics*. John Wiley & Sons, 488p
- Karakus M, Perez S (2014) Acoustic emission analysis for rock–bit interactions in impregnated diamond core drilling. *Int J Rock Mech Min Sci* 68:36–43
- Kidambi T, Kumar GS (2016) Mechanical earth modeling for a vertical well drilled in a naturally fractured tight carbonate gas reservoir in the Persian Gulf. *J Pet Sci Eng* 141:38–51
- Lashkaripour GR, Rastegarnia A, Ghafoori M (2018) Assessment of brittleness and empirical correlations between physical and mechanical parameters of the Asmari limestone in Khersan 2 dam site, in southwest of Iran. *J Afr Earth Sci* 138:124–132
- Li X, Yan X, Kang Y (2017) Investigation of drill-in fluids damage and its impact on wellbore stability in Longmaxi shale reservoir. *J Pet Sci Eng* 159:702–709
- Maleki S, Gholami R, Rasouli V, Moradzadeh A, Riabi RG, Sadaghzadeh F (2014) Comparison of different failure criteria in prediction of safe mud weigh window in drilling practice. *Earth Sci Rev* 136:36–58
- Mehrabi H, Rahimpour-Bonab H (2014) Paleoclimate and tectonic controls on the depositional and diagenetic history of the Cenomanian–early Turonian carbonate reservoirs, Dezful Embayment, SW Iran. *Facies* 60(1):147–167
- Mehrabi H, Rahimpour-Bonab H, Hajikazemi E, Jamalnia A (2015) Controls on depositional facies in Upper Cretaceous carbonate reservoirs in the Zagros area and the Persian Gulf, Iran. *Facies* 61(4):23
- Mehrgini B, Memarian H, Dusseault MB, Eshraghi H, Goodarzi B, Ghavidel A, Qamsari MN, Hassanzadeh M (2016) Geomechanical characterization of a South Iran carbonate reservoir rock at ambient and reservoir temperatures. *J Nat Gas Sci Engin* 34:269–279
- Mogi K (1971) Effect of the triaxial stress system on the failure of dolomite and limestone. *Tectonophysics* 11(2):111–127
- Mohr O (1900) Welche Umstände bedingen die Elastizitätsgrenze und den Bruch eines Materials. *Zeitschrift des Vereins Deutscher Ingenieure* 46(1524–1530):1572–1577
- Motiei H., 1993. *Stratigraphy of Zagros*. Treatise on the Geology of Iran, 151p. In Persian
- Nabaei M, Moazzeni AR, Ashena R, Roohi A (2011) Complete loss, blowout and explosion of shallow gas, infelicitous horoscope in Middle East. In: SPE European Health, Safety and Environmental Conference in Oil and Gas Exploration and Production
- Najibi AR, Ghafoori M, Lashkaripour GR, Asef MR (2015) Empirical relations between strength and static and dynamic elastic properties of Asmari and Sarvak limestones, two main oil reservoirs in Iran. *J Pet Sci Eng* 126:78–82
- Najibi AR, Ghafoori M, Lashkaripour GR, Asef MR (2017) Reservoir geomechanical modeling: in-situ stress, pore pressure, and mud design. *J Pet Sci Eng* 151:31–39
- Omidvar M, Mehrabi H, Sajjadi F, Bahramizadeh-Sajjadi H, Rahimpour-Bonab H, Ashrafzadeh A (2014) Revision of the foraminiferal biozonation scheme in Upper Cretaceous carbonates of the Dezful Embayment, Zagros, Iran: integrated palaeontological, sedimentological and geochemical investigation. *Rev Micropaleontol* 57(3): 97–116
- Plumb RA (1994) Influence of composition and texture on the failure properties of clastic rocks. In *Rock Mechanics in Petroleum Engineering*, Society of Petroleum Engineers
- Rahimpour-Bonab H, Mehrabi H, Navidtalab A, Izadi-Mazidi E (2012) Flow unit distribution and reservoir modelling in cretaceous carbonates of the Sarvak formation, Abteymour oilfield, Dezful Embayment, SW Iran. *J Pet Geol* 35(3):213–236
- Rahimpour-Bonab H, Mehrabi H, Navidtalab A, Omidvar M, Enayati-Bidgoli AH, Sonei R, Sajjadi F, Amiri-Bakhtyar H, Arzani N, Izadi-Mazidi E (2013) Palaeo-exposure surfaces in Cenomanian–santonian carbonate reservoirs in the Dezful Embayment, SW Iran. *J Pet Geol* 36(4):335–362
- Rajabi M, Sherhati S, Bohloli B, Tingay M (2010) Subsurface fracture analysis and determination of in-situ stress direction using FMI logs: an example from the Santonian carbonates (Ilam formation) in the Abadan Plain, Iran. *Tectonophysics* 492(1):192–200
- Roegiers JC (2002) Well modeling: an overview. *Oil Gas Sci Technol* 57(5):569–577
- Santarelli FJ, Detienne JL, Zundel JP (1989) Determination of the mechanical properties of deep reservoir sandstones to assess the likelihood of sand production. In: ISRM International Symposium. International Society for Rock Mechanics
- Yaghoobi AA, Zeinali M (2009) Determination of magnitude and orientation of the in-situ stress from borehole breakout and effect of pore pressure on borehole stability—case study in Cheshmeh Khush oil field of Iran. *J Pet Sci Eng* 67(3):116–126
- Zhang J (2011) Pore pressure prediction from well logs: methods, modifications, and new approaches. *Earth Sci Rev* 108(1):50–63
- Zhang L, Cao P, Radha KC (2010) Evaluation of rock strength criteria for wellbore stability analysis. *Int J Rock Mech Min Sci* 47(8):1304–1316
- Zhou J, He S, Tang M, Huang Z, Chen Y, Chi J, Zhu Y, Yuan P (2018) Analysis of wellbore stability considering the effects of bedding planes and anisotropic seepage during drilling horizontal wells in the laminated formation. *J Pet Sci Eng*
- Zoback MD (2010) *Reservoir geomechanics*. Cambridge University Press, 449p
- Zoback MD, Barton CA, Brudy M, Castillo DA, Finkbeiner T, Grollmund BR, Moos DB, Peska P, Ward CD, Wiprut DJ (2003) Determination of stress orientation and magnitude in deep wells. *Int J Rock Mech Min Sci* 40(7):1049–1076